

# How Electron Localization Function Quantifies and Pictures Chemical Changes in a Solid: The B3 → B1 Pressure Induced Phase Transition in BeO

J. Contreras-García, A. Martín Pendás, and J. M. Recio\*

Departamento de Química Física y Analítica, Universidad de Oviedo, E-33006 Oviedo, Spain

Received: January 23, 2008; Revised Manuscript Received: May 12, 2008

Advantages of the analysis of the topology of the electron localization function (ELF) in the characterization of the chemical bonding in solids are illustrated in the study of the zinc blende → rock salt transformation in BeO. The 4-fold to 6-fold coordination change is described as a two-step process: first, a catastrophic-like emergence of two new Be–O bonds reveals the onset of the rock salt structure, and second, the new interactions gradually evolve to achieve the bonding network of the high-pressure phase. The increase in coordination, the volume collapse and the enhancement in the bulk modulus across the transition pathway are qualitatively and quantitatively traced back to the oxygen's valence shell. Although several ELF indexes point toward the expected greater bond polarity in the B3 than in the B1 structure, it can be concluded that there is no substantial modification in the nature of the crystal interactions induced by the phase transformation.

## I. Introduction

Characterization of chemical changes induced by thermodynamic variables in crystals is of capital interest in a variety of scientific areas from fundamentals in solid state chemistry to applications in materials science.<sup>1,2</sup> It covers structural, energetic, and bonding understanding of the local environment of the atomic constituents of solids and involves the modifications within the same crystalline structure or between different polymorphs if a solid–solid phase transition occurs. Detailed information on the geometry and phase stability dependence on pressure and temperature of different crystal structures is currently available from X-ray and/or neutron diffraction experiments and computer assisted simulations.<sup>3,4</sup> On the other hand, interphase phenomena should usually resort to martensitic-like or molecular dynamics models describing the mechanism of transformation, and their validity ultimately relies on the comparison with the data of the observed phase transition properties.<sup>5,6</sup>

In both intra- and interphase phenomena in solids, the chemical bonding appears as a central topic toward which many efforts are currently invested to reconcile the traditional picture derived from Lewis theory with the outcome of first principles quantum-mechanical methodologies.<sup>7</sup> Quantitative and rigorous formalisms based on the topological analysis of scalar fields related to the electron density ( $\rho(\vec{r})$ ) have been successfully used in the molecular realm, but their application in the solid state has been less frequent (see ref 8 for a review).

In this respect, the electron localization function (ELF) provides the foundation for a rich characterization of the chemistry of compounds that merits to be exploited in detail. It is a local measure of electron localization within a system based on Pauli's principle. As initially developed by Becke and Edgecombe, the ELF ( $\eta(\vec{r})$ ) quantifies the conditional probability of finding an electron in the neighborhood of another one with the same spin.<sup>9</sup> This initial definition is difficult to apply to solid state problems, because it involves using second-order density matrices that are not easily available. This drawback was overcome when Savin proposed an interpretation of Becke's

formula in terms of the difference between the local kinetic energy of the system ( $t(\vec{r})$ ) and that of a noninteracting one (von Weizsäcker term) to account for the excess of kinetic energy due to the Pauli repulsion.<sup>10</sup> Only local one-electron properties, namely the definite positive kinetic energy, the electron density and its derivatives, are needed. The usual ELF formula normalizes this excess to the kinetic energy density of a homogeneous electron gas of the same electron density ( $c_F\rho^{5/3}$ ,  $c_F$  is the Fermi constant) and then maps it to the (0,1) interval:

$$\eta(\vec{r}) = \left[ 1 + \frac{\left( t(\vec{r}) - \frac{|\nabla\rho|^2}{8\rho} \right)^2}{c_F\rho^{5/3}} \right]^{-1} \quad (1)$$

High  $\eta(\vec{r})$  regions are associated with increased electron pair localization. In this way, the topology induced by the ELF field provides an exhaustive partition of the space into basins, each of them containing one of the so-called ELF attractors of maxima. Experience has shown that the ELF basins are associated with atomic shells, lone pairs and bonds.<sup>7</sup> As pointed out by Gillespie and Robinson,<sup>11</sup> the ELF exhibits maxima at the most probable positions of localized electron pairs and each maximum is surrounded by a basin in which there is an increased probability of finding an electron pair. These basins correspond to the qualitative electron pair domains of the VSEPR (Valence Shell Electron Pair Repulsion) and have the same geometry as the VSEPR domains. Besides, in the solid state this kind of exhaustive partition has the advantage of enabling a unequivocal assignation of basin contributions to many properties of the solid.<sup>12</sup>

Two topological entities need to be determined for this purpose, the maxima and the basin separatrices. The latter task has hampered the development of ELF topological analysis in solids due to serious problems imposed by periodicity. The program CRITIC,<sup>13</sup> initially developed in our laboratory for the analysis of the electron density topology in crystals under the atoms in molecules (AIM) formalism,<sup>14,15</sup> has been recently extended to make thorough ELF analysis available to crystalline solids. CRITIC is now able to completely characterize both the AIM and ELF topologies of periodic systems of any nature and

\* Corresponding author. E-mail: mateo@fluor.quimica.uniovi.es.

then to use these results to determine the zero flux surfaces of  $\rho$  and  $\eta$ , and to integrate density operators, such as charge density or volume, within them.<sup>16</sup>

It is one of our aims in this work to illustrate how the ELF analysis can contribute to the understanding of the behavior and properties of crystals under hydrostatic pressure. BeO is a simple binary compound with elements of the first row of the Periodic Table where our code is expected to work accurately. Although it has not been observed yet, 4-fold tetrahedrally coordinated Be is theoretically predicted to transform to the 6-fold octahedral environment of the rock salt (*B1*) structure when hydrostatic pressure is applied in the range of approximately 100 GPa.<sup>17,18</sup> Whether this pressure induced phase transition involves wurtzite (*B4*) or zinc blende (*B3*) as the low pressure phase is not especially relevant for the purpose of our work. Both structures display similar local atomic environments and very similar energetics and equations of state.<sup>19</sup>

We particularly focus our investigation on the chemical changes of BeO in the wurtzite, zinc blende and rock salt structures, and across the *B3*  $\rightarrow$  *B1* transition pathway. The mechanism of the latter transformation has been extensively studied in a number of II–VI and III–V binary compounds using a diffusionless and martensitic perspective, and it has been concluded that an orthorhombic *Imm2* unit cell provides a rational physical description with a low activation barrier between the two structures.<sup>20–23</sup> This fact together with the structural simplicity of *B3* drove us to choose this phase instead wurtzite in our study. Our goal here is to gain insight in the process of creation of the new atomic coordination that takes place across the transition. We want to know if the 6-fold coordination found in the high pressure phase appears from the beginning or emerges at a later stage. We also investigate how these changes correlate with the energetic profile and the atomic displacements involved in the transformation. Such correlations are crucial for a global understanding of the phase transition mechanism.

The rest of the paper is divided in three more sections. First, we describe computational details associated with the electronic structure calculations and with the capacity of our ELF analytical code. Second, we organize the presentation and discussion of the response to hydrostatic pressure of the structure and chemical bonding in BeO in two subsections dedicated to intra- and interphase properties, respectively. Finally, we summarize the main conclusions derived from our work along with some future prospects in the last section.

## II. Computation of ELF Topology: Charges and Volumes of Basins

Static total energy ( $E$ ) calculations at a number of volumes ( $V$ ) in the wurtzite, zinc blende, and rock salt unit cells were carried out under the generalized gradient approximation (GGA) of the density functional formalism using Perdew and Wang<sup>24</sup> electronic exchange–correlation functional. We have followed a rather standard plane-wave pseudopotential scheme as implemented in the Vienna ab initio package (VASP).<sup>25</sup> A  $8 \times 8 \times 8$  Monkhorst–Pack<sup>26</sup> grid was chosen to generate the sampling  $k$ -points and an energy cutoff of 520 eV to ensure convergence of the total energy within  $10^{-3}$  eV. One internal coordinate and the  $c/a$  ratio need to be optimized in wurtzite, whereas in the cubic cells of zinc blende and rock salt no structural optimizations are required as Be and O stand at fixed positions.

Numerical and analytical (Vinet)<sup>27</sup> equations of state were used to describe ( $E$ ,  $V$ ) points of the three structures to provide pressure ( $p$ )– $V$  data, equation of state (EOS) parameters (bulk

modulus,  $B_0$ , and its pressure derivative,  $B_0'$ , both evaluated at zero pressure), and enthalpy ( $H$ )– $p$  curves.  $H$  is the appropriate thermodynamic potential to determine phase stability at static conditions (zero temperature and zero point vibrational contributions neglected). These calculations have been performed with the GIBBS code.<sup>28</sup> The zinc blende  $\rightarrow$  rock salt transition mechanism has been studied under a total energy martensitic approach following a transition pathway of *Imm2* symmetry, which is a subgroup common to the conventional unit cells of the *B3* and *B1* structures. This transition path involves the optimization of three parameters to determine the intermediate transition structures using the  $z$  coordinate of Be ( $z_{\text{Be}}$ ) as the transformation coordinate.<sup>22</sup>

An all electron wave function is needed for a reliable and quantitative analysis of the ELF topology in a crystalline phase. Our new computational code of ELF analysis in solids has been interfaced to the CRYSTAL98 package<sup>29</sup> from which all electron crystalline wave functions of BeO have been computed. The optimized structures obtained with VASP were, therefore, recalculated with the CRYSTAL98 code to obtain all electron wave functions for the three polymorphs and the transition structures. Optimized Be and O basis sets were chosen from previous calculations<sup>30</sup> for zinc blende and wurtzite structures, whereas for the rock salt structure the most diffuse exponent was reoptimized ( $\zeta = 0.238$ ). We have checked that the ELF topological analysis across the transition path is not modified by this basis set alternative. We have tried to follow as much as possible the same type of calculation and equivalent computational parameters as in the VASP calculations. This strategy has been successfully carried out in our previous topological analysis of the electron density in a variety of high pressure studies of halide, oxide and nitride crystals.<sup>31</sup>

The ELF topology and the properties of the basins of the rock salt and zinc blende structures have been studied at several pressures from 0 to around 100 GPa. Similar analysis were carried out for the calculated transition structures across the zinc blende  $\rightarrow$  rock salt *Imm2* transition pathway. The enormous number of critical points of the ELF field in a solid, as well as the low symmetry of some of the basins associated to their maxima, leads to serious difficulties if we seek for a quantitative analysis of its topology, and more specifically in the case we are interested here, the physical and chemical changes induced on the ELF topology by hydrostatic pressure. Making use of automatized and efficient recursive algorithms, our code is able to provide an accurate analysis and characterization of all the critical points of the ELF surface. They are usually classified as maxima (attractors, (3,−3)), minima (cages, (3,+3)), and first-order (bonds, (3,−1)), and second-order (rings, (3,+1)) saddle points. The first-order saddle points along with the maxima are used to construct the bifurcation tree<sup>32,33</sup> and to perform an analysis of interbasin relationships. Once the attractors have been located, the separatrices of their basins are found by means of a bipartition procedure.<sup>34</sup> Basin properties are calculated by integrating appropriate density operators, i.e., charge density, over the basins. Basin populations have been converged to the hundredths of electron, which requires the use of  $30 \times 20$  radial and angular grids. Finally, graphical representations of the set of critical points and the basins are available in 1-, 2- and 3-dimensions in common visualization formats. Tessel<sup>35</sup> and Molekel<sup>36</sup> packages have been used through this paper for 3-D representation of the ELF in these structures.

## III. Results and Discussion

**A. ELF Analysis of *B3* and *B1* Polymorphs of BeO.** Our VASP calculated zero pressure structural and EOS parameters

**TABLE 1: Structural and EOS Parameters of Wurtzite (B4), Zinc Blende (B3), and Rock Salt (B1) Structures of BeO**

	B4			B3		B1	
	present	ref 17 <sup>a</sup>	ref 37 <sup>b</sup>	present	ref 17 <sup>a</sup>	present	ref 17 <sup>a</sup>
<i>a</i> (Å)	2.710	2.703	2.698	3.825	3.810	3.649	3.648
<i>c/a</i>	1.625	1.620	1.622				
<i>d</i> <sub>Be-O</sub> (Å)	1.655	1.651	1.654	1.656	1.650	1.825	1.824
$\Delta E$ (meV)				13	14	912	1075
<i>B</i> <sub>0</sub> (GPa)	211	203	212	215	201	240	231
<i>B</i> <sub>0</sub> '	3.8		4 (fixed)	3.6		4.0	

<sup>a</sup> DFT-GGA calculations. <sup>b</sup> X-ray diffraction experiments.

of B4, B3, and B1 phases of BeO along with previous theoretical and experimental data are gathered in Table 1. Only the wurtzite phase has been observed in high pressure experiments up to 55 GPa.<sup>37</sup> The calculated properties for this phase are in very good agreement with the experimental data. Wurtzite is 13 meV lower in energy than zinc blende at zero pressure according to our calculations. Energy differences between these two structures are negligible in the whole range of pressure studied in this work (up to 150 GPa). Wurtzite and zinc blende display very similar Be–O distances and EOS parameters. At zero pressure, both structures are more compressible than B1, display shorter Be–O bond lengths, and lower density. This is the expected trend attending to the number of nearest neighbors. In both coordinations, BeO exhibits higher *B*<sub>0</sub> values than other binary oxides of group IIa. The same behavior is found in other headgroup compounds if we compare, for example, LiF and BN with binary fluorides of group Ia and binary nitrides of group IIIa, respectively.

All these results are very similar to those of Park et al.<sup>17</sup> using the same level (GGA) of calculation. Other representative theoretical calculations carried out in BeO in the last ten years are reported in refs 17–19 and 38. Park et al.<sup>17</sup> discuss in detail the cohesive properties of the three polymorphs of BeO including comparisons with local density approximation (LDA) calculations and other theoretical approaches. As our main concern here is the ELF analysis of the chemical bonding in 4-fold and 6-fold BeO structures, we will not analyze these results further and we will concentrate in the ELF topology of B3 and B1 polymorphs.

Attractors and bond points (from now on bond interaction points, *bips*) for BeO in the zinc blende and the rock salt structures are shown in Table 2. Results for the wurtzite phase are very similar to the ones of zinc blende. The first outstanding feature of the ELF analysis is that the electron pairs are distributed in both structures, forming closed atomic electronic shells around the nuclei: one shell for beryllium (the core K-shell, K(Be)) and two for oxygen (the core K-shell, K(O) and the valence L-shell, L(O)). There are no electrons associated with bonding basins. Therefore, the ELF analysis clearly classifies the bonding in both structures as ionic. Second, the most striking figure to a reader familiar with ELF analysis might be the occurrence of several valence maxima within one shell. It should be noted that there are four Be and four O atoms in the unit cell, and that the multiplicities (*M*) of the L(O) attractors are 16 (B3) and 24 (B1) (see *N* = 3 in Table 2). This fact, however, is a direct consequence of the symmetry of the cell and the atomic positions. Furthermore, this shell splitting can be directly associated with the nearest neighbors interactions because the oxygen L shell is divided into four and six equivalent basins in the zinc blende and rock salt structures, respectively, with the positions of the attractors standing on

O–Be directions. This can be easily inferred from the coordinates of the L(O) maxima in Table 2.

Therefore, the initially spherical valence shell of an oxygen atom in vacuo has developed into four (B3) or six (B1) equivalent attractors (*N* = 3). This may be seen as incipient frustrated bond basins. It is also possible to rationalize this image in terms of partial condensation of electron pairs. The four (B3) or six (B1) Be atoms surrounding a given oxygen atom thus define preferent directions of partial electron pairing. Notice also how this partial condensation is slightly enhanced in the B3 phase, because the  $\eta(N=3)$  value is higher in this case. This is also related to bond polarity issues (see below).

A closer look at the L(*i*(O))–L(*j*(O)) (3,–1) critical points (*N* = 5) enables us to recover the traditional chemical image of a O<sup>2–</sup> ion. *i* and *j* refer to two of the basins in which the L(O) shell is divided. When the ELF value at the *bips* closely matches the value at the maxima (0.845 and 0.863 in B3, and 0.844 and 0.852 in B1), the basins should be regarded as forming one superbasin which in this case surround the K(O) shell displaying the widespread contouring L shell picture.<sup>39,40</sup> It is also to be noted that the ELF analysis reveals a weak interaction between the anions, as already found in other ionic compounds using also the AIM formalism.<sup>41,42</sup> The link between L basins associated with two different oxygen atoms takes place here through L(O<sub>*i*</sub>)–L(O<sub>*j*</sub>) *bips* of low  $\eta$  values (*N* = 6) in both structures. Thus, the basins associated with the L shell of each oxygen form one superbasin that might be understood as a unique chemical entity.

This analysis can be more formally carried out through the construction of the corresponding bifurcation diagram. To do that, we only have to follow increasing  $\eta$  values at the *bips* (see the scheme in Figure 1). This diagram reveals the interbasin relationships. The pattern confirms in both structures the ionic picture: the crystal is divided into Be<sup>2+</sup> and O<sup>2–</sup> ions before core and valence of the anions are reduced. The following steps are somehow more interesting: as already explained before, the basins (L<sub>*i*</sub>, L<sub>*j*</sub>) from a common L oxygen shell are to be considered as one and so they split up at really high ELF values. But before that occurs, there is a separation of the contiguous nearest oxygen atoms (O<sub>*i*</sub>, O<sub>*j*</sub>) surrounding Be at  $\eta$  around 0.085, which is followed by the oxygen core–valence separation. In summary, because the electrons are only localized forming closed shell electronic structures with very weak relationships between basins on different ions, we can conclude that the stabilization of B3 and B1 BeO phases is mainly due to the genuine electrostatic interactions of ionic compounds that result from the beryllium to oxygen charge transfer.

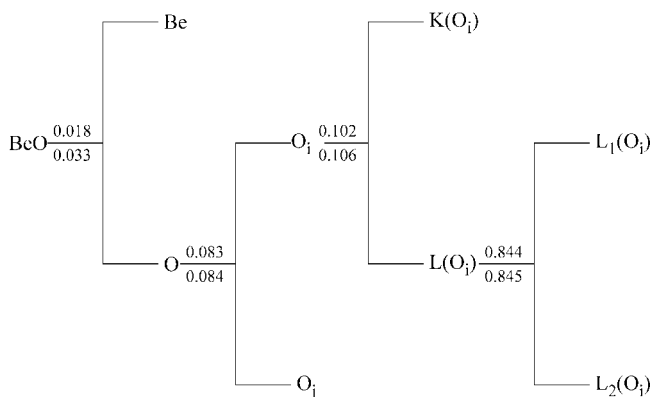
Our next step deals with the quantification of this transference. The volumes (*v<sub>i</sub>*) and charges (*q<sub>i</sub>*) associated to each of the basins have been calculated. The partition of real space into localized basins allows us to divide a given crystal property,  $\omega$ , into basin contributions:  $\omega = \sum f_i \omega_i$ , being *f<sub>i</sub>* the fractional volume occupation of the *i*th basin in the unit cell.<sup>12</sup> Results for the integrals over volume and population have been carried out for the shell basins of BeO in B3 and B1 structures, and are shown in Table 3. It can be seen that, in both phases, we are dealing with an ionic compound where a charge transfer of around 1.94 electrons yields approximately Be<sup>2+</sup> and O<sup>2–</sup> ions. It is noteworthy that electron integrals are very close to the nominal values of 2 and 8 electrons for K and L shells, respectively. This is a clear proof of the quantitative ability, besides the qualitative ones, of the electron localization function. Furthermore, relative errors in the total number of electrons and unit cell volumes are always lower than 1%.



**TABLE 2:  $\eta$  Values and Coordinates of the ELF Attractors and Bond Interaction Points Found for the  $B3$  ( $a = 3.825$  Å) and  $B1$  ( $a = 3.649$  Å) Structures of BeO at Zero Pressure<sup>a</sup>**

<i>N</i>	<i>B3</i>							<i>B1</i>						
	$\eta$	type	<i>x</i>	<i>y</i>	<i>z</i>	<i>M</i>	CHM	$\eta$	type	<i>x</i>	<i>y</i>	<i>z</i>	<i>M</i>	CHM
1	1.000	(3,−3)	0.000	0.000	0.000	4	K(O)	1.000	(3,−3)	0.000	0.000	0.000	4	K(O)
2	1.000	(3,−3)	0.250	0.250	0.250	4	K(Be)	1.000	(3,−3)	0.000	0.000	0.500	4	K(Be)
3	0.863	(3,−3)	0.095	0.095	0.095	16	L(O)	0.852	(3,−3)	0.000	0.000	0.335	24	L(O)
4	0.106	(3,−1)	0.032	0.032	0.032	16	K(O)–L(O)	0.102	(3,−1)	0.000	0.000	0.058	24	K(O)–L(O)
5	0.845	(3,−1)	0.000	0.000	0.154	24	L <sub><i>i</i></sub> (O)–L <sub><i>j</i></sub> (O)	0.844	(3,−1)	0.000	0.387	0.387	48	L <sub><i>i</i></sub> (O)–L <sub><i>j</i></sub> (O)
6	0.084	(3,−1)	0.029	0.250	0.250	24	L(O <sub><i>i</i></sub> )–L(O <sub><i>j</i></sub> )	0.083	(3,−1)	0.000	0.201	0.201	48	L(O <sub><i>i</i></sub> )–L(O <sub><i>j</i></sub> )
7	0.033	(3,−1)	0.174	0.174	0.174	16	K(Be)–L(O)	0.018	(3,−1)	0.000	0.000	0.351	24	K(Be)–L(O)

<sup>a</sup> *M* and CHM stand for the multiplicity and chemical meaning of the critical point, and subscripts *i* and *j* denote either two equivalent basins or two different oxygen atoms.

**Figure 1.** ELF bifurcation diagram of  $B3$  and  $B1$  phases of BeO. Numbers above ( $B3$ ) and below ( $B1$ ) of basin bifurcations stand for  $\eta$  values at the corresponding *bips*.**TABLE 3: Zero Pressure Charges, Volumes, and Bulk Moduli of BeO Basins According to Present ELF Analysis<sup>a</sup>**

	<i>B3</i>			<i>B1</i>		
	<i>q<sub>i</sub></i>	<i>v<sub>i</sub></i>	<i>B<sub>i</sub></i>	<i>q<sub>i</sub></i>	<i>v<sub>i</sub></i>	<i>B<sub>i</sub></i>
K(Be)	2.06	4.529	404	2.05	5.053	468
K(O)	2.14	0.273	4340	2.14	0.274	5907
O	9.94	89.681	197	9.94	76.496	231
$\epsilon$ (%)	0.0	−0.2	−6.0	−0.1	−0.5	3.2

<sup>a</sup> Units of *q<sub>i</sub>*, *v<sub>i</sub>*, and *B<sub>i</sub>* are *e*, bohr<sup>3</sup>, and GPa, respectively.

The oxygen's valence accounts for almost 95% of the unit cell volume in the two structures. Moreover, the difference in volume of the  $B3$  and  $B1$  structures at zero pressure (around 13%) is almost entirely assumed by the L(O) basin. This change also appears at the  $B3$ – $B1$  transition pressure and will be analyzed across the transition pathway in the next subsection. Hence, the L(O) basins are expected to undergo maximal changes under pressure. Therefore, and in concordance with chemical intuition, the ELF is able to identify the anion valence as the main responsible for the pressure response of the solid. To quantify this effect, integrals have been carried out over a range of pressures and the equation of state (EOS) of each phase divided into basin contributions:

$$\kappa = -\frac{1}{V} \frac{\partial V}{\partial p} = \sum f_i \kappa_i \quad (2)$$

where  $\kappa_i = -(1/v_i)(\partial p/\partial v_i)$  defines the basin compressibility.<sup>12,43</sup> The Vinet EOS nicely fits the  $p$ – $v_i$  data of K(Be) and L(O) basins, but for the smaller and less pressure sensitive K(O) basins the values collected in Table 3 are only indicative. Notice that the weight of K(O) in the final value of the bulk compressibility is almost negligible. Our calculations show that,

in fact, the oxygen's valence compressibility is responsible for more than 90% of the volume reduction of BeO under pressure. It is also interesting to note that Be cores show a simultaneous slight volume increment, probably related to the increase in coordination upon transition. The comparison between  $B_0$  values in Table 1 with the ones computed with eq 2 ( $\kappa = 1/B_0$ ) (Table 3) is very satisfactory with deviations around 6% or lower. It can be concluded that the enhanced compressibility of the  $B3$  phase is a direct consequence of the greater volume of the oxygen valence shell in this structure due to the lower number of nearest neighbors. This can be easily checked recalling to the bulk modulus-volume inverse relationship<sup>44</sup> because the zero pressure bulk modulus of the  $B1$  phase can be approximately recovered using the volumes of oxygen in both phases in this equation:

$$B_0^{B1} = \frac{v_O^{B3}}{v_O^{B1}} B_0^{B3} \quad (3)$$

Once we have posed the general results of the ELF analysis in BeO, we detail particular differences of the bonds in the  $B3$  and  $B1$  structures. It has long been recognized that the polarity of the Be–O bonds is responsible for the special features BeO presents when compared to its homologues in the II–VI series. We have found that its bond in zinc blende and rock salt structures is ionic in nature, with an almost complete charge transfer in both cases. How does ELF account for the polarity of BeO and for its change across the transition? The polarity of a bond is usually pictured as an oriented deformation of the electron density concentration between the bonded atoms toward the more electronegative one.

Although the oxygen's basin is rather spherical in both  $B3$  and  $B1$  phases of BeO, ELF provides a clear view of the onset of polarity in these ionic compounds. As explained above, the Be atoms force a partial pair condensation of the electrons along Be–O directions. This is the origin of the splitting of L(O) into four ( $B3$ ) and six ( $B1$ ) associated basins, which together deviate slightly from sphericity. This phenomenon is easily visualized in Figure 2, where we plot 6, 6, and 4 subshells corresponding to the splitting of the anion's valence shell due to the environment of LiF ( $B1$ ), BeO ( $B1$ ), and BeO ( $B3$ ) lattices. Solid spheres represent the cations (red and fuchsia for Li<sup>+</sup> and Be<sup>2+</sup>, respectively), whereas ELF isosurfaces at the  $\eta$  value of the corresponding valence intrashell *bip* (brown for F and grey for O) surround the anion cores (brown for F and blue for O). It can be seen how the six valence basins of F in the  $B1$  phase of LiF almost reconstruct a spherical surface surrounding the anion. On the other hand, the deformation of the L(O) basin in BeO is clearly visible and noticeably larger in the  $B3$  phase where a tetrahedron shape is observed. Comparing zinc blende and rock

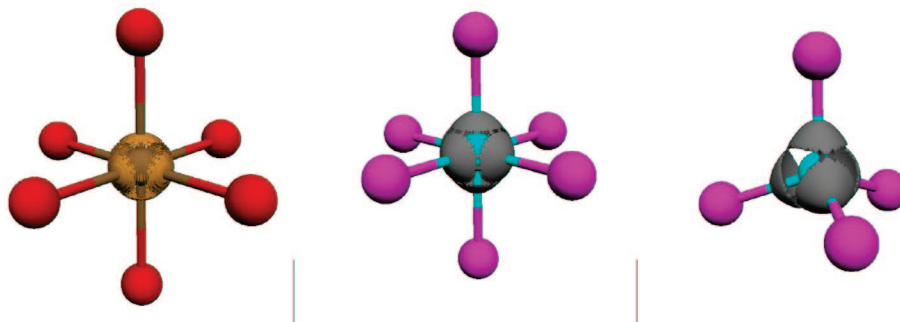


**Figure 2.** From left to right, isosurfaces of the valence ELF at the *bip* value for LiF, BeO (*B1*) and BeO(*B3*).

**TABLE 4: Polarity Indexes**

index	LiF	BeO ( <i>B1</i> )	BeO ( <i>B3</i> )
$\Delta\eta^{\text{val}}$	0.0003	0.008	0.018
$\lambda_1$	-1.1427	-0.76018	-0.71516
$\lambda_2$	$-0.5413 \times 10^{-2}$	$-0.786 \times 10^{-1}$	-0.1181
$\Delta r$	0.0012	0.0181	0.0413

salt BeO, it becomes obvious how polarization is decreased for the high pressure phase. This interpretation of polarity enables the visualization and quantification of the delocalization induced by pressure.

To quantify these effects, the validity of several indexes has been revised and/or analyzed. First, Silvi and Gatti<sup>45</sup> proposed the following delocalization index for measuring the delocalization within a metallic structure:

$$\Delta\eta^{\text{val}} = \eta_{(3,-3)}^{\text{val}} - \eta_{(3,-1)}^{\text{val}} \quad (4)$$

It was conceived as the ELF difference between the maxima and first-order saddle point of the valence basins. This index can be adapted and recovered as a polarity index if the critical points taken into account are the maxima of the ionic valence and the saddle points of the *intra*-valence shell:

$$\Delta\eta^{\text{val}} = \eta_{(3,-3)}^{\text{val}} - \eta_{(3,-1)}^{\text{val}} \quad (5)$$

Values for  $\Delta\eta^{\text{val}}$  (see Table 4) confirm the expected trend. It is also interesting to examine the Lyapunov exponents,  $\lambda_1$  and  $\lambda_2$  at the valence attractor, which account for the deformation of the localization *bip* surfaces toward the nearest neighbor atoms.  $\lambda_1$  is the greatest Hessian eigenvalue of ELF at the (3,−3) point, and its eigenvector naturally points toward the neighboring atom. Greater values of  $\lambda_1$  are associated with larger ELF curvatures along the Be–O axis, weaker relationship between bonded basins and a smaller covalent character. The eigenvector associated with  $\lambda_2$ , on the other hand, shows the direction of maximal perpendicular ELF curvature. Strongly ionic cores, being spherical, will show very low  $\lambda_2$  values, as can be seen for LiF in Table 4. As bond polarization increases, this value will also increase (such is the case of BeO). Finally, and very intuitively, it is possible to measure the deformations from sphericity by using the difference in distance from the nucleus to the valence attractor (3,−3) and to the saddle point, an index that will grow in magnitude as the ion departs from sphericity:

$$\Delta r^{\text{val}} = r_{(3,-3)}^{\text{val}} - r_{(3,-1)}^{\text{val}} \quad (6)$$

It is interesting to note how all these indexes collected in Table 4 are able to account for the differential polarity, already seen in Figure 2, of the *B1* and *B3* phases in a simple and physically rooted manner. Needless to say, these indexes should be used mindfully. The nearly same atomic radius of the species here compared ( $r_{\text{BP}} \approx 2.3$  bohr) allows direct comparison of

their delocalization values. Rigorous relationships between elements from different periods would require rescaling to the atomic radii. Extra care is also advised in the use of  $\Delta\eta^{\text{val}}$  for nonrelated chemical species. The mapping introduced in the seminal definition of ELF gives rise to a nonlinear relationship of the chemically meaningful quantity  $((t(r) - t_w(\vec{r}))/c_{\text{FP}})^{5/3}$  with ELF increments. In summary, and to the best of our knowledge, it is the first time that quantitative indexes have been proposed to specifically measure the polarity of ionic crystals thanks to the ELF, softening the dicotomic view of bonds (ionic vs covalent) it offers.

**B. ELF Analysis Across the *B3* → *B1* Phase Transition Mechanism.** Pressure ranges of phase stability and phase transition properties of BeO have shown to be more sensitive to the computational level/approach of calculation than intraphase properties. This is a common feature of ab initio calculations: properties are relatively stable against perturbations in regions of topological stability, whereas small changes close to catastrophic turning points, resulting from different methodological approaches, give rise to great quantitative changes. In spite of their hypothetical character, *B4* → *B3* (see refs 17–19), *B4* → *B1* (see refs 18, 19, and 38), and *B3* → *B1* (see refs 17 and 18) phase transitions have also been characterized and discussed previously. For example, Cai et al.<sup>18</sup> used the relative slopes of *B3* and *B4*  $H(p)$  calculated curves along with a calculated activation barrier for the *B4* → *B3* transformation to rule out the *B3* phase in the pressure induced polymorphic sequence of BeO. We understand that temperature also plays an important role to overcome such a barrier and that BeO could finally be present in the zinc blende structure.

Our calculations indicate that zinc blende becomes stable with respect to wurtzite at 116 GPa. In fact, the three structures show very similar enthalpy values in the 110–120 pressure range (in GPa) and it is not possible to resolve the precise thermodynamic sequence within the present modeling parameters. In previous works, this range (in GPa) is 76.2–94.1 (ref 19), 91.2–147.1 (ref 17), and 87–105 (ref 18). For the purpose of our study, it is worthwhile to point out that both, previous and present calculations, clearly reveal the occurrence of a 4-fold to a 6-fold transformation induced by pressure at around 100 GPa. According to our VASP calculations, changes in volume and bulk modulus relative to the low pressure phase and associated with the corresponding phase transition are almost negligible for the *B4* → *B3* transformation and around 11% for the volume and 6% for *B* when the coordination changes from 4-fold to 6-fold. We again observe that our calculated absolute and relative *V* and *B* values of the structures involved in these transitions are consistent with previous available data and with the trends of other II–VI compounds considering that Be and O are the lightest elements of their respective groups.

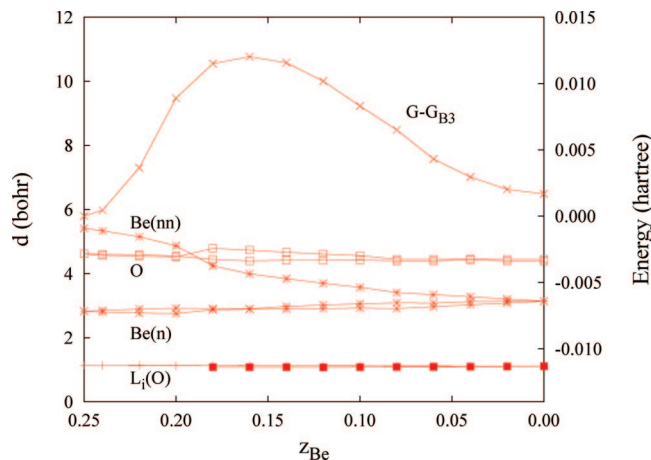


**Figure 3.** Gibbs energy profile and distances from oxygen to oxygen valence attractors ( $L_i(O)$ ), nearest ( $Be(n)$ ) and next nearest ( $Be(nn)$ ) Be atoms, and O nearest atoms across the transition path at  $p$  close to the transition pressure. New oxygen basins (bold squares) emerge at  $z_{Be} = 0.18$  and  $z_{Be} = 0.10$ .

We now focus on the  $B3 \rightarrow B1$  transition pathway. Using an orthorhombic *Imm2* unit cell, Miao and Lambrecht have demonstrated the universal character of relevant structural and energetic properties involved in this transformation for a number of II–VI semiconductors.<sup>22</sup> The energetic profile of the transition path can also be shown to be universal if scaled with the corresponding activation barrier ( $\Delta G^\ddagger$ ). This is defined as the difference between the Gibbs energy at the maximum of the energetic profile (the transition state,  $\ddagger$ ) and the Gibbs energy of the  $B3$  or  $B1$  phases.<sup>5</sup> The appropriate transformation coordinate under the generalized Landau theory for reconstructive phase transitions<sup>46</sup> is the  $z$  coordinate of Be ( $z_{Be}$ ), which changes from 0.25 ( $B3$ ) to 0.00 ( $B1$ ). Cai et al.<sup>23</sup> have recently supported the usefulness of this *Imm2* space group to describe the  $B3 \rightarrow B1$  transition path in GaAs. Results for BeO are examined here for the first time and are in very good agreement with the previous work in other binary compounds. Although this is not the goal of our study, this description is a necessary step to introduce the ELF analysis and to look for a connection between structure, bonding, and energy across the transition path.

In brief, our results locate the transition state at  $z_{Be} = 0.16$ , with an energy barrier of around 0.30 eV. Our calculated  $c/a$ ,  $b/a$  and  $V/V_{B3}$  curves across the *Imm2* pathway (not shown here) follow the same pattern as the one displayed by the binary compounds examined in refs 22 and 23. Taking one O atom of the  $B3$  phase as the reference center, the atomic reorganization is easily visualized as due to two new Be atoms approaching from the next nearest Be coordination shell to the nearest Be coordination shell. These two equivalent Be atoms are initially around 2.6 Å away from the nearest coordination shell, and suffer a change in distance with respect to the reference O atom of about 2.3 Å, because the shortest Be–O distance is 0.3 Å larger in the  $B1$  than in the  $B3$  phase. How this change takes place across the transition path is illustrated in Figure 3 for a pressure slightly below the transition pressure. Curves for the distance from oxygen to its valence attractors, for the shortest O–O distances, and for the Gibbs energetic profile (relative to the Gibbs energy of the  $B3$  phase,  $G_{B3}$ ) are also displayed in Figure 3. We observe that O–Be and O–O curves show continuous and soft trends except, perhaps, for the pronounced decrease of the distance of the two approaching Be atoms just before the transition state is reached. This behavior is related to the appearance of new L(O) basins and is explained below.

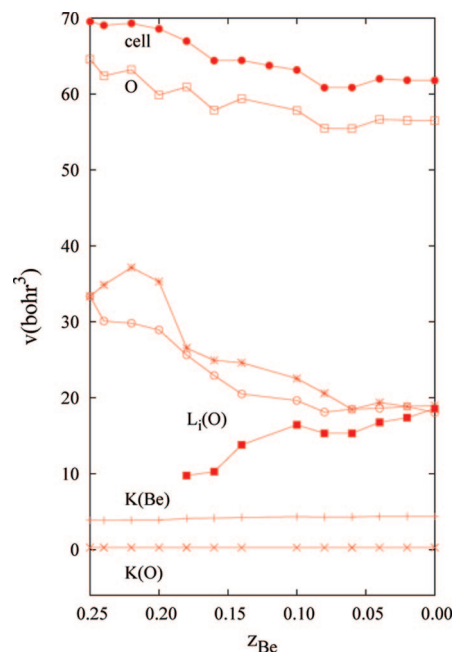


**Figure 4.** Volumes of core and valence basins, oxygen (K+L), and unit cell ( $Z = 1$ ) along the transition path. New oxygen basins (bold squares) emerge at  $z_{Be} = 0.18$  and  $z_{Be} = 0.10$ .

The ELF topological analysis across the transition path clearly reveals that all the relevant chemical changes are suffered by the O valence, which goes from 2 to 3 sets of symmetrically non equivalent basins. This topological change proceeds in two steps. First, the new pair of approaching Be atoms induces the appearance of a new valence basin associated with oxygen atoms: a cusp catastrophe transforms the  $(3, -1)$  critical point into one attractor and two new first-order  $(3, -1)$  critical points. The formation of the new basins occurs around  $z_{Be} = 0.18$  (see Figure 5), i.e., close to the transition state, and reveals the onset of the new phase. To analyze whether the process is only due to a geometrical (distance) effect or not, we have carried out the following computational experiment. A cluster model consisting of a central  $O^{2-}$  ion surrounded by five  $Be^{2+}$  ions in the vertices of an octahedron, and at the same distances found in the zero pressure  $B1$  structure of BeO, is used to examine the appearance of a new valence attractor when a sixth  $Be^{2+}$  approaches the cluster along the direction of the empty vertex of the octahedron. As expected from the periodic solid results, a valence attractor appeared in the direction of the approaching  $Be^{2+}$  at a Be–O distance of about 4.00 bohr, which corresponds to  $z_{Be} \approx 0.18$  (see Figure 3). Hence, the valence reorganization taking place along the  $B3 \rightarrow B1$  transition is to be viewed as a limited redistribution of the regions of partial condensation of pairs and not as a full chemical bond change.

Second, the new attractor is initially located along the plane that bisects the angle formed by the O atom and the two approaching Be atoms. As the Be atoms approach the oxygen ( $z_{Be} = 0.10$ ), this initial attractor is divided into two corresponding to the new O–Be bonds. Furthermore, the new oxygen L-shell basins, very small in electron population and volume at the beginning, evolve across the transition so that they resemble the other four. This means that a second cusp catastrophe changes the new L-shell attractor into one  $(3, -1)$  critical point and two new attractors. At the end, the valence is divided into three pairs of equivalent basins, perfectly showing the change in coordination occurring in the crystal (see Figure 5). The  $B1$  conformation is achieved at  $z_{Be} = 0.0$ , when all three sets



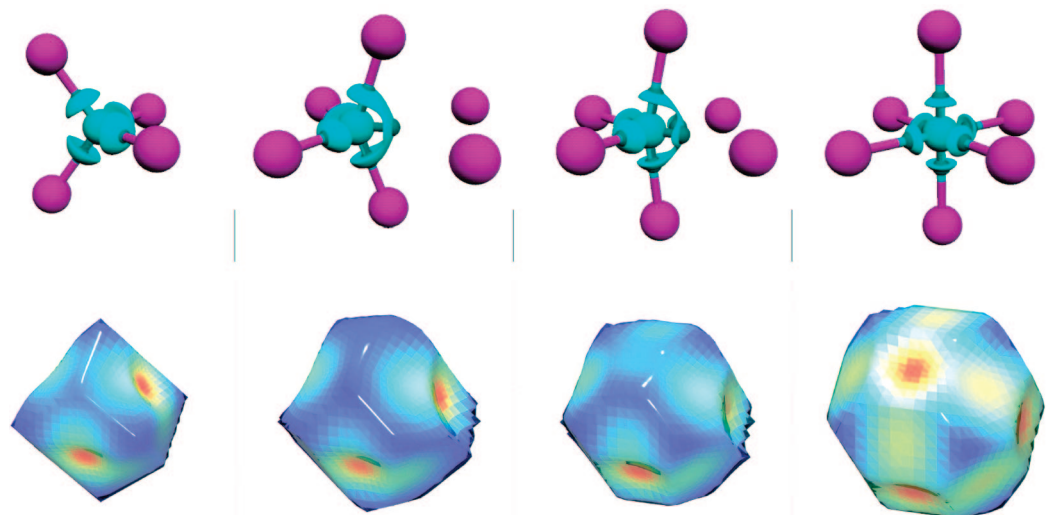


**Figure 5.** Evolution of ELF profiles (top) and  $\rho$  oxygen basins (bottom) across the  $B3 \rightarrow B1$  phase transition at  $z_{\text{Be}}$  values of 0.25, 0.18, 0.10, and 0.00.  $\text{Be}^{2+}$  core ELF surfaces in fuchsia,  $\text{O}^{2-}$  core and valence ELF surfaces in light blue. Attractors of the  $\text{O}^{2-}$  ELF valence basin are displayed in dark blue. Values of the electron density at the zero flux surfaces increase from blue to red.

become equivalent. In summary, the bonding process across the transition path is topologically split in three domains of structural stability: the first one displays 4-fold coordination ( $z_{\text{Be}} > 0.18$ ), the second one 5-fold coordination ( $0.18 > z_{\text{Be}} > 0.10$ ), and the last one 6-fold coordination ( $z_{\text{Be}} < 0.10$ ). The Be and O cores remain practically untouched across the transition path. This is illustrated in the two top curves of Figure 4, where we clearly observe that the cell volume and the total oxygen volume follow very similar trends.

Furthermore, the topological changes induced in the electron density basins of O have been depicted for comparison in the low row of Figure 5. It can be seen how the associated polyhedra describe the change from 4-fold phase  $B3$  to 6-fold phase  $B1$ . However, in this case, the change in coordination takes place in one step at  $z_{\text{Be}} = 0.10$ , where one new bond point appears directed to each of the approaching Be. The deformation of the ions toward sphericity (Figure 5) is apparent and suggests the use of geometrical indexes for quantifying the ionic character of the Be–O bond. The global picture remains the same as the one derived from the ELF analysis. The increasingly positive curvature associated to the eigenvector tangent to the new bond path ( $\lambda_3$ ) and the decreasing negative value of the perpendicular ones ( $\lambda_1, \lambda_2$ ) add up to give a positive Laplacian at the new bond point (signature of an ionic bonding). The value of the Laplacian increases slightly along the transition path (from 0.2673 at  $z_{\text{Be}} = 0.10$  to 0.4433  $z_{\text{Be}} = 0.00$ ).

The 4-fold to 6-fold change is classified according to the bond evolution theory as polymorphic (the number of basins increases) and would identify the process taking place as chemical in nature.<sup>47,48</sup> However, the question arises whether this definition does also apply to basins which are chemically significant as a whole. Although the different extent of preferential pair condensation, as illustrated in Figure 2 and quantified in Table 4, can be interpreted as some kind of detectable chemical change associated with the transformation, it is our point of view that the catastrophic change merely reflects the change in coordination, because all the basins involved represent the same chemical entity and should be taken as one superbasin. There is a topological change, but it corresponds to the same basic chemical picture, an ionic compound whose polarity softly changes as measured by the above delocalization indexes, but whose partial charge concentrations only reflect coordination.

#### IV. Conclusions and Some Prospects

A thorough quantitative topological analysis of the electron localization function in a solid phase transition has been for the first time put forward thanks to the application of a new computational code. A deep study of the  $B3$  and  $B1$  phases of BeO has been carried out, with a complete topological and chemical characterization of the critical points set. The general features of ELF crystalline basins have been identified. With this at hand, the phase transition from one polymorph to the other has been tracked under a martensitic approach, showing that no fundamental changes in the bonding pattern occur and that ELF clearly reveals the energetic and structural changes taking place. A step toward the understanding of polarity in the ELF framework has been taken, showing that atomic sphericity is substituted by deformed ELF basins when polarity is increased. An effect that can be easily visualized and quantified, both for different compounds and for phases.

Our next step toward a deeper understanding of the processes taking place within solids is to carry out the analysis of phase transitions where a change in the nature of the bond occurs. Work is in progress in both  $\text{CO}_2$  and  $\text{SiO}_2$ , where the change from molecular to covalent and polar-ionic networks awakes much interest due to the natural relevance of both compounds. To provide a nonambiguous tool to understand these changes in the bond nature, we are currently working in the development of a user-friendly index that would quantify the nature of these chemical bonds in terms of the ELF topological analysis.

**Acknowledgment.** Financial support from the Spanish MEC and FEDER program under project MAT2006-13548-C02-02 and the Spanish MALTA-Consolider Ingenio-2010 (CSD2007-00045) are gratefully acknowledged. J.C.G. thanks the Spanish MEC for a FPU postgraduate grant. Part of this work was performed during the stays of J.M.R. (under a HPC-EUROPA grant) and J.C.G. at the Laboratoire de Chimie Théorique (Université Pierre et Marie Curie, Paris). Thanks are due to Prof. B. Silvi for his wise advice and constant encouragement.

#### References and Notes

- (1) Grochala, W.; Hoffmann, R.; Feng, J.; Ashcroft, N. W. *Angew. Chem., Int. Ed.* **2007**, *46*, 3620.

- (2) Leoni, S. *Chem. Eur. J.* **2007**, *13*, 10022.
- (3) Nemes, R. J.; McMahon, M. I. In *Semiconductors and Semimetals*; Suski, T., Paul, W., Eds.; Academic: New York, 1998; Vol. 54, p 145.
- (4) Mujica, A.; Rubio, A.; Munoz, A.; Needs, R. J. *Rev. Mod. Phys.* **2003**, *75*, 863.
- (5) Martín Pendás, A.; Recio, J. M.; Francisco, E.; Luana, V. *Phys. Rev. B* **1997**, *56*, 3010.
- (6) Oganov, A. R.; Ono, S. *Nature* **2004**, *430*, 445.
- (7) Silvi, B.; Savin, A. *Nature* **1994**, *371*, 683.
- (8) Gatti, C. Z. *Kristallogr.* **2005**, *220*, 399.
- (9) Becke, A.; Edgecombe, K. E. *J. Chem. Phys.* **1990**, *92*, 5397.
- (10) Savin, A.; Jepsen, O.; Flad, J.; Andersen, O. K.; Preuss, H.; von Schnering, H. G. *Angew. Chem., Int. Ed.* **1992**, *31*, 187.
- (11) Gillespie, R. J.; Robinson, E. A. *J. Comput. Chem.* **2007**, *28*, 87.
- (12) Martín Pendás, A.; Costales, A.; Blanco, M. A.; Recio, J. M.; Luana, V. *Phys. Rev. B* **2000**, *62*, 13970.
- (13) Martín Pendás, A.; Luana, V. The CRITIC program, 1995–2000.
- (14) Bader, R. F. W. *Atoms in Molecules*; Oxford University Press: Oxford, U.K., 1990.
- (15) Martín Pendás, A.; Costales, A.; Luana, V. *Phys. Rev. B* **1997**, *55*, 4275.
- (16) Contreras-García, J.; Martín Pendás, A.; Silvi, B.; Recio, J. M. *J. Phys. Chem. Solids*, DOI: 10.1016/j.jpcs.2008.03.028.
- (17) Park, C. J.; Lee, S. J.; Ko, Y. J.; Chang, K. J. *Phys. Rev. B* **1999**, *59*, 13501.
- (18) Cai, Y.; Wu, S.; Xu, R.; Yu, J. *Phys. Rev. B* **2006**, *73*, 184104.
- (19) Boettger, J. C.; Wills, J. M. *Phys. Rev. B* **1996**, *54*, 8965.
- (20) Sowa, H. Z. *Kristallogr.* **2000**, *215*, 335.
- (21) Catti, M. *Phys. Rev. Lett.* **2001**, *87*, 035504.
- (22) Miao, M. S.; Lambrecht, W. R. L. *Phys. Rev. Lett.* **2005**, *94*, 225501.
- (23) Cai, J.; Chen, N.; Wang, H. J. *Phys. Chem. Solids* **2007**, *68*, 445.
- (24) Perdew, J. P.; Wang, Y. *Phys. Rev. B* **1992**, *45*, 13244.
- (25) Kresse, G.; Furthmüller, J. *Phys. Rev. B* **1996**, *54*, 11169.
- (26) Monkhorst, H. J.; Pack, J. D. *Phys. Rev. B* **1976**, *13*, 5188.
- (27) Vinet, P.; Rose, J. H.; Ferrante, J.; Smith, J. R. *J. Phys.: Condens. Matter* **1989**, *1*, 1941.
- (28) Blanco, M. A.; Francisco, E.; Luana, V. *Comput. Phys. Commun.* **2004**, *158*, 57.
- (29) Saunders, V. R.; Dovesi, R.; Roetti, C.; Causá, M.; Harrison, N. M.; Orlando, R.; Zicovich-Wilson, C. M. *CRYSTAL98 User's Manual*; University of Torino: Torino, 1998.
- (30) Lichanot, A.; Chaillet, M.; Lairreu, C.; Dovesi, R.; Pisani, C. *Chem. Phys.* **1992**, *164*, 383.
- (31) Marqués, M.; Osorio, J.; Ahuja, R.; Flórez, M.; Recio, J. M. *Phys. Rev. B* **2004**, *70*, 104114.
- (32) Silvi, B.; Savin, A.; Colonna, F. *Can. J. Chem.* **1996**, *74*, 1088.
- (33) Calatayud, M.; Andrés, J.; Beltrán, A.; Silvi, B. *Theor. Chem. Acc.* **2001**, *105*, 299.
- (34) Biegler-König, F. W.; Bader, R. W.; Tang, T. J. *Comput. Chem.* **1982**, *3*, 317.
- (35) <http://web.uniovi.es/qcg/tessel/tessel2f.html>.
- (36) , Flükeger, P.; Lüthi, H. P.; Portmann, S.; Weber, J. *MOLEKEL*; Swiss National Supercomputing Centre: Manno, Switzerland.
- (37) Hazen, R. M.; Finger, L. W. *J. Appl. Phys.* **1986**, *59*, 3728.
- (38) Van Camp, P. E.; Van Doren, V. E. *J. Phys.: Condens. Matter* **1996**, *8*, 3385.
- (39) Silvi, B. *J. Mol. Struct.* **2002**, *614*, 3.
- (40) Mori-Sánchez, P.; Recio, J. M.; Silvi, B.; Sousa, C.; Martín Pendás, A.; Luana, V.; Illas, F. *Phys. Rev. B* **2002**, *66*, 075103.
- (41) Mori-Sánchez, P.; Martín Pendás, A.; Luana, V. *J. Am. Chem. Soc.* **2002**, *124*, 14721.
- (42) Martín Pendás, A.; Costales, A.; Luana, V. *Phys. Rev. B* **1998**, *55*, 4275.
- (43) Recio, J. M.; Franco, R.; Martín Pendás, A.; Blanco, M. A.; Pueyo, L.; Pandey, R. *Phys. Rev. B* **2001**, *63*, 184101.
- (44) Hazen, R. M.; Finger, L. W. *J. Geophys. Res.* **1979**, *84*, 6723.
- (45) Silvi, B.; Gatti, C. J. *Phys. Chem.* **2000**, *104*, 247.
- (46) Dmitriev, V. P.; Rochal, S. B.; Gufan, Y. M.; Toledano, P. *Phys. Rev. Lett.* **1988**, *60*, 1958.
- (47) Krokidis, X.; Noury, S.; Silvi, B. *J. Phys. Chem. A* **1997**, *101*, 7277.
- (48) Polo, V.; Andres, J.; Castillo, R.; Berski, S.; Silvi, B. *Chem. Eur. J.* **2004**, *10*, 5165.